Materials for life sciences

An injectable, self-healing and degradable hydrogel scaffold as a functional biocompatible material for tissue engineering applications

Shengyu Li[1,3,4,*] (iD), Weiye Mao[1,4], Linying Xia[2], Xijin Wu[1,4], Yingxue Guo[1,4], Jingwei Wang[1,3], Jie Huang[1,4], Hai Xiang[3], Lu Jin[1,4], Huiying Fu[1,3,4], and Qiyang Shou[1,3,4,*]

[1] The Second Affiliated Hospital Second Clinical Medical School of Zhejiang Chinese Medical University, Hangzhou 310000, China

[2] Basic Medical Sciences of Zhejiang Chinese Medical University, Hangzhou 310005, China

[3] Jinghua academy of Zhejiang Chinese Medicine University, Jinghua 321015, China

[4] Zhejiang Provincial Key Laboratory of Sexual function of Integrated Traditional Chinese and Western Medicine, Hangzhou 310053, China

ABSTRACT

Injectable hydrogels derived from natural extracellular matrices exhibit excellent adhesion to endothelial cells in vitro and are ideal for many biomedical applications. However, their applicability in vivo is limited by the risk of infection or immunogenicity, and the current injectables also suffer from degradation, viscosity, and drug release. In this study, a multifunctional hydrogel scaffold (COB hydrogels) was constructed by incorporating bioactive glass nanoparticles with a Schiff base crosslinking-based hydrogel composed of carboxymethyl chitosan and oxidized cellulose. The incorporation of nanoparticles not only shortened the gelation time of the COB hydrogels, but also enhanced the performance of the hydrogel in terms of function, such as drug loading capacity. The prepared hydrogels also have self-healing ability, injectability, drug loading and sustained release, antibacterial properties and biocompatibility. In addition, given their no cytotoxicity and mild inflammation in vivo, the hydrogel scaffolds will be important for tissue engineering and drug delivery applications.

https://doi.org/10.1007/s10853-023-08393-8

Introduction

Hydrogels' structural and mechanical properties are similar to the extracellular matrix of natural tissues, and can provide sufficient biochemical signals to support cell attachment, proliferation, and differentiation. So, hydrogels are one of the important biomaterials for scaffold fabrication [1, 2]. In addition, hydrogels can be divided into natural polymer-based hydrogels and synthetic polymer-based hydrogels because of their raw material sources [3]. Among them, hydrogels with injectable properties are the latest research achievements in this field [4, 5]. Injectable hydrogels are a kind of functional materials that can be injected into the target site by syringe. These materials have a wide range of application prospects in tissue filling and repair, drug delivery, bleeding sealing, biological scaffolds and other fields as they are minimally invasive, adapting to irregular defect edge filling [6–9].

Recently, the Schiff base crosslinking reaction have been widely studied for their various simplicity, reversibility and avoidance of chemical crosslinking agents and biocompatibility [10, 11]. Chitosan is a simple multifunctional material, which has been widely applied in several fields, such as environmental energy, biomaterials, and biomedicine [12, 13]. Carboxymethyl cellulose (CC), a major cellulose derivative, is widely used in biomedical applications owing to its biocompatibility, low toxicity, low cost, and remarkable optical properties [14–17].

Hydrogel composites comprising functional biocompatible nanoparticles (NPs) have been applied to drug delivery and tissue engineering purposes [18, 19]. NPs can be loaded with specific drugs to enhance their therapeutic capacity and improve drug bioavailability [20, 21]. Moreover, the chemical properties of NPs can induce numerous biological reactions, such as the antibacterial activity of silver nanoparticles [22], antioxidant property of gold nanoparticles [23], and regulation of some specific cell types (for example, calcium-based nanoparticles regulating keratinocyte migration [24]). In recent years, bioactive glass nanoparticles (BGN) have been widely used as inorganic materials in medical research [25]. Kim et al. and Li. et al. claimed that drug-free BGN could achieve profound anti-inflammatory effects in vivo [26, 27]. Moreover, BGNs have

the advantages of a high surface area, surface functionality, low toxicity, and combined pharmacotherapy [28]. Overall, BGNs have been proved to have a great potential for tissue engineering applications.

In this work, we designed and prepared an injectable hydrogel scaffold based on carboxymethyl chitosan and cellulose derivatives and loaded with bioactive nanoparticles. Unlike currently designed soft tissue fillers, the developed hydrogel scaffold combines important advantages such as (i) self-healing ability, (ii) drug loading and sustained release, (iii) degradability, (iv) antibacterial property, (v) no cytotoxicity, (vi) mild inflammation in vivo. It indicated that COB hydrogels are great potential in future clinical applications.

Experimental

Materials

Dodecylamine (DDA, 98%), tetraethyl orthosilicate (TEOS, 98%), triethyl phosphate (TEP, 98%), sodium carboxymethyl cellulose (CC, 300–800 CP) and Doxorubicin (Dox) were purchased from Aladdin (Shanghai, China). Calcium nitrate tetrahydrate and Ethylene glycol (99%) was purchased from Huadong Medicine and 9-Ding Chemistry respectively. Carboxymethyl chitosan (CMCs) was purchased from Macklin (Shanghai, China) and the degree of substitution was greater than 80%. Sodium periodate ($NaIO_4$, 99%) and 2, 4-dihydroxybenzaldehyde (98%) were purchased from Sinopharm chemical reagent (Shanghai, China) and ZhongHe chemical Technology respectively (Shanghai, China). Hydroxylammonium chloride was purchased from Sigma-Aldrich (St. Louis, MO, USA). Medical Sodium Hyaluronate Gels (Haifeile) were purchased from the local hospital. No other treatments are required for these reagents. Water used in experiments (DW) was purified using a Millipore water purification system with a minimum resistivity of 18.0 MΩ cm.

Preparation and characterization of BGN

Monodispersed mesoporous bioactive glass was synthesized by an improved sol–gel method using dodecylamine (DDA) as the catalyst and template. Briefly, 0.08 M DDA was dissolved in 80% ethanol solution. After DDA was completely dissolved, 16 ml

of TEOS and 1.22 of mL TEP were added and stirred for 30 min at 40 °C. Subsequently, 3.39 g of CN was then added and stirred for 3 h at 40 °C. The collected white precipitate was rinsed three times with anhydrous ethanol and deionized water and freeze-dried for 24 h. Next, the powder was calcined in a high temperature muffle furnace (Honglong Instrument Equipment Factory, MF, Nanjing) at 650 °C for 3 h at 2 °C/min to remove the templates and organic components in the BGNs calcination. The chemical composition of BGN was observed and analyzed using an energy-dispersive X-ray spectrometer (EDS, SU8010, Hitachi Limited, Japan). At 77.3 K, the specific surface area and pore volume were evaluated using the multipoint Brunauer-Emmett–Teller (BET) N_2 absorption technique. The pore size was also calculated using the Barrett–Joyner–Halenda (BJH) method [29]. The particle size distributions of the samples were tested using a Malvern Zeta Sizer Nano S-90 dynamic light scattering (DLS) instrument. After immersion in a simulated buffer solution (SBF), the formation of apatite on the surface of BGN was evaluated through Field Emission Scanning Electron Microscopy (FE-SEM, SU8010, Hitachi Limited, Japan) equipped with an energy-dispersive X-ray spectrometer (EDS) to confirm the biomineralized bioactivity of BGN.

Synthesis and characterization of oxidized CC (OCM)

Different molar ratios of $NaIO_4$ (4:1, 3:1, 2:1, 1:1) and CC solution (1 wt%, dissolved in 100 ml deionized water) were stirred overnight in the dark conditions at 25 °C to obtain oxidized CC with appropriate oxidation degree. Subsequently, 1 ml ethylene glycol was added to remove any unreacted $NaIO_4$. The solution was dialyzed in distilled water for three days and lyophilized to obtain the product (defined as OCM_{25}, OCM_{50}, OCM_{75}, OCM_{100} in terms of oxidation ratio). The aldehyde group content was quantified by measuring the number of aldehyde groups in the fibers. The oxidation degree was determined by titration of hydrochloric acid produced by the reaction of aldehyde group and hydroxylamine hydrochloride (Fig. 1a) [17, 30]. The oxidation degree of OCM_{25}, OCM_{50}, OCM_{75}, OCM_{100} was 12.77±1.912%, 38.96±4.12%, 62.5±3.72%, 75.03 ±5.57% respectively (Table S2, supporting information). The structure of the OCM was further

confirmed using a Thermo Scientific K-Alpha spectrometer and Fourier transform infrared spectrometer (Thermo Fisher Nicolet iS50, Thermo Fisher Scientific Co., Ltd., USA). X-ray photoelectron spectra (XPS) provided relevant information about the type of functional groups on the OC_{25} and OC_{100}. As shown in Fig. 1c, three characteristic peaks of C1s, N1s and O1s were observed on the surface of materials. The C1s XPS spectrum of OC_{25} (i) and OC_{100} (ii) in the inset was deconvoluted into four peaks at 284.6 eV, 286.4 eV, 287.1 eV and 288.4 eV, corresponding to C–C, C=N, C–OH, and C=O, respectively [31]. The intensity of OC_{100} in the C1s region at 288.4 eV was higher than that of OC_{25}, confirming that OC_{100} had more aldehyde groups. This result was consistent with the estimated aldehyde content of hydroxylamine hydrochloride method. In contrast to CC, a characteristic peak of aldehyde groups around 2900 cm^{-1} was observed in the spectrum of OCM (Fig. S2). Moreover, this peak intensity increased with the degree of oxidation.

Fabrication of COB hydrogels

For rapid bonding, a higher degree of oxidation (OCM_{100}) was selected to crosslink with CMCs. BGN was uniformly dispersed in deionized water (DW) at a final concentration of 0.5, 1 and 1.5 wt% under agitation and ultrasonic waves. Meanwhile, CMCs was dissolved in BGN suspension at a final concentration of 5 wt% and the prepared OCM_{100} was dissolved in DW at concentration of 15 wt%. Finally, OCM_{100} solution and CMCs solution with or without BGNs were mixed evenly at volume ratio of 1:1 to form COB hydrogels by a dual barrel syringe. The obtained samples are named as COB_y. y stands for the concentration of BGN.

Characterization of COB hydrogels

The surface morphology and chemical composition of hydrogels samples were observed and analyzed by a FE-SEM and X-ray energy spectrum (EDS). The interaction of Schiff bases in hydrogels was studied using X-ray photoelectron spectroscopy (XPS) performed by Thermo Scientific K-Alpha spectrometer. The X-ray diffraction (XRD) patterns of the samples were analyzed by an X-ray diffractometer (XRD-7000, Shimadzu, Japan) in a continuous mode with 2θ scanned from 10° to 80°. Fourier Transform infrared
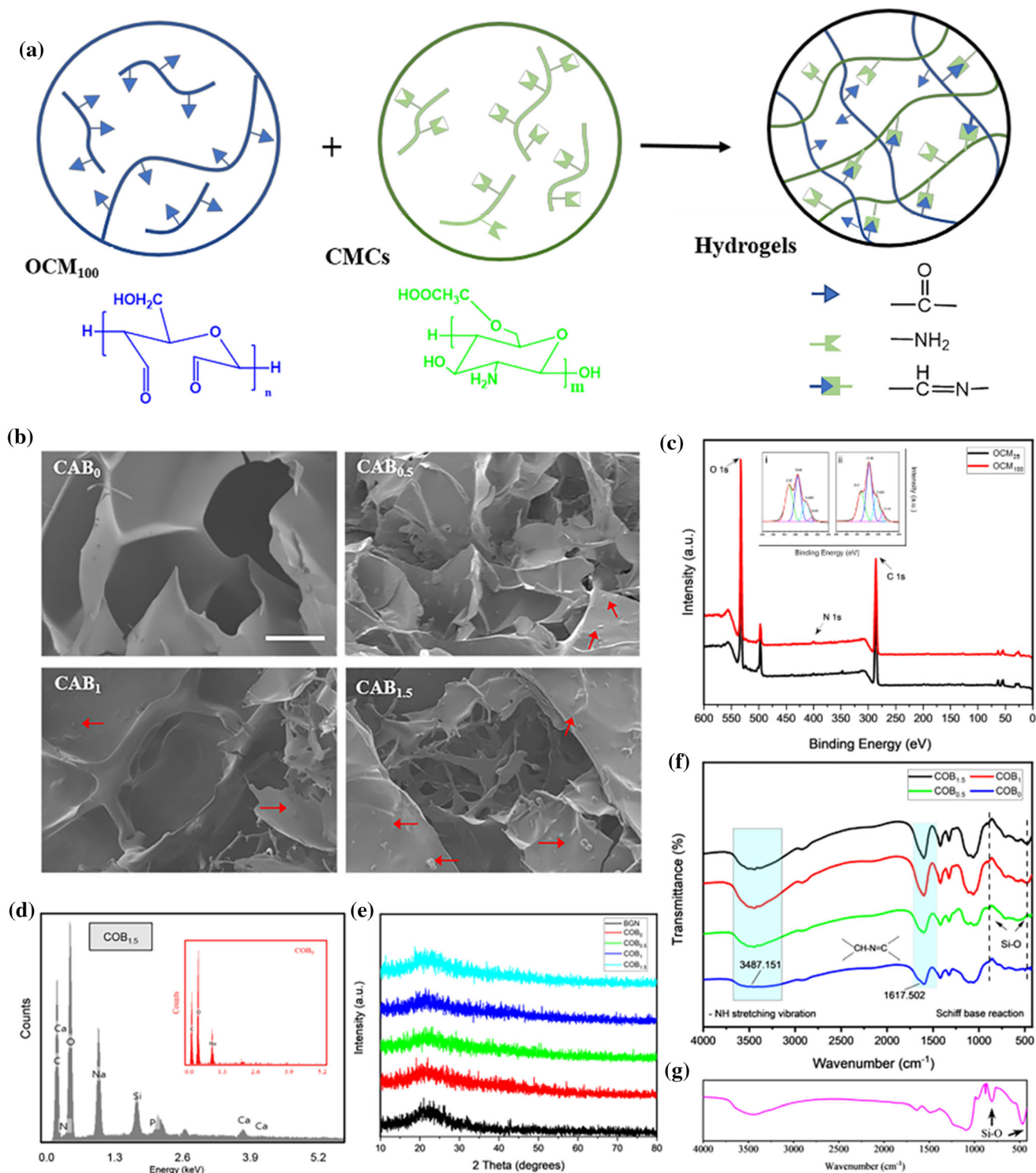
Figure 1 a The illustration of Schiff base reaction between OCM_{100} and CMCs. **b** FE-SEM micrographs of COB_0, $COB_{0.5}$, COB_1 and $COB_{1.5}$. The red arrows mark BGN, scale bar=50 μm. **c** XPS spectra of the OC_{25} and sample OC_{100}, C 1 s spectra of OC_{25} (**i**), and OC_{100} (**ii**). **d** The EDS of COB hydrogels. **e** XRD patterns showing the amorphous structure of COB hydrogels. The FTIR spectrum of **f** COB hydrogels and **g** BGN, the arrow points to the Si–O characteristic peak.

spectroscopy (FTIR) analysis of COB gels were recorded with FTIR spectrometer (Thermo Fisher Nicolet iS50, Thermo Fisher Scientific Co., Ltd., USA) against a blank KBr pellet background. The light transmittance of gels was measured with a UV–Vis Spectrophotometer (SHIMADZU UV-2550, Shimadzu Instrument Co., Ltd. China).

The water loss rate and EWC of COB hydrogels

The water loss rate: the hydrogels were allowed to swell equilibrium in PBS (pH 7.4) and weighed (initial weight, W_d). Then placed them at 37 °C to lose water. At a given time period, the hydrogels were weighed, which were recorded as W_t, and water loss rate is calculated as follows: The water loss rate (%)= W_d/W_t*100%.

The equilibrium water content: firstly, the fully swollen hydrogel samples were weighed as Ws. Subsequently, the hydrogels were dehydrated via lyophilized and weighted (W_i). The equilibrium water content (EWC) was expressed as: EWC (%)= $(W_s-W_i)/W_s$*100%. All experiments were repeated for three times.

Self-healing behavior and injectable property of hydrogels

Two slices of freshly cut hydrogels (COB_0) were placed in proximity in a closed environment for 12 h at room temperature. The hydrogels were then placed on a hollow platform and bent with the fingers into a "U" shape to better demonstrate the self-healing behavior of the gel. The mechanical properties of COB_0 hydrogels with were characterized by Electronic Universal Testing Machine (WDW-5D, Jinan Wenteng Testing Instrument Co., Ltd., China). In the compression experiment, a cylindrical hydrogel with 15 mm in diameter and 10 mm in height was set on the lower plate and compressed by the upper plate at a strain rate of 10 mm/min. In addition, the mechanical properties of the healing hydrogel were also measured by the same method. Degree of recovery relative to its original state and used to quantify healing performance: $\eta=P_{healed}/P_{origin}$. Where P is the mechanical strength [32].

The hydrogel stained with black ink was sprayed with a double syringe at the rate of 0.2 ml/s to observe its injectable ability. All of these tests were recorded by a camera, and the corresponding photographs are presented in this paper.

In vitro bonding strength

Fresh porcine skin was cut into rectangular pieces. Solutions (100 μL of CMCs solution and 100 μL of OCM_{100}) were spread over two skin slices. The skin sections were then overlapped to a 1.5×1.5 cm^2 adhesive area. After placing a weight (100 g) at the bonding point for 5 min, the bonding strength of the porcine skin was measured using a universal testing machine. The tests were performed at least three times, and the average strength was measured. The negative controls consisted of simple CMCs.

In vitro biodegradability of hydrogels

The COB hydrogels (500 μg) were initially weighed and then immersed in 10 mM PBS pH 7.4 at 37 °C, which were recorded as W_0. At a given time period, the hydrogels were taken out and removed surface moisture, then weighed as W_t. After every 12 h, the PBS was replaced with same volume of new one. The degradation rate was calculated as follows: The degradation rate (%)= W_t/W_0*100%.

Drug loading and release of hydrogels

Lyophilized hydrogels were immersed in a solution containing 500 μg/ml doxorubicin (DOX) at room temperature. After 48 h, 2 ml of the supernatant was collected and the ultraviolet spectra were measured at 300 to 800 nm, and the UV wavelength of DOX was approximately 480 nm. The amount of the loaded drug was estimated by subtracting the presence of DOX in the supernatant from the control concentration.

The doxorubicin-loaded hydrogels were immersed in 1 ml of PBS. At specific times (4 h, 8 h,10 h, 12 h, 24 h, and 48 h), 1 ml of the release medium was collected and replaced with the same amount of fresh PBS. The presence of DOX in the release medium was quantitatively determined using UV spectroscopy.

Rheology

Dynamic rheological tests of the hydrogels were conducted by a Rheometer ARES-G2 (TA-Waters, USA) strain-controlled rheometer equipped with 8

mm parallel plates. Frequency sweep experiments were performed on each sample (COB_0, $COB_{0.5}$, COB_1 and $COB_{1.5}$) in the range at an angular velocity of $0.01 \sim 100$ Hz to determine the dynamic storage modulus (G′) and loss modulus (G″) with constant strain of 25 rad^{-1} at 25°C.

Cell culture on the hydrogels and CCK-8 assay

NIH 3T3 cells (Cell Biolabs Inc.) in passage three was used for seeding onto UV-sterilized hydrogels (COB_0, $COB_{0.5}$, COB_1, $COB_{1.5}$, 0.05 g/ml). Cells were inoculated in a 24-well plate with a concentration of 3×10^4 cells/well and cultured in a humidified incubator (5% CO_2) at 37 °C. The CCK-8 assay was used to evaluate cell proliferation after 1 day of culture. The relative cell viability was calculated as follows:

$$\text{Cell viability} = \frac{\text{OD sample} - \text{OD blank}}{\text{OD control} - \text{ODblank}} * 100\%$$

Cell's state was observed by a fluorescence microscope (ECLIPSE TI-S, Nikon, Japan) after stained with Calcein—AM/PI.

Bacterial colony assay

The antibacterial activity of the COB gels against the gram-negative bacterium *E. coli* and the gram-positive bacterium *S. aureus* was investigated. In brief, the bacteria were diluted in 0.9% physiological saline to reach a concentration of 1×10^6 CFU/ml. The bacterial suspension solutions (100 µL/well) were then added to a 96-well plate. Samples of the same quality were added to the board and the culture plate was cultured at 37 °C for 4 h. Then The solution in the 96-wells were diluted with PBS, placed on LB agar plates, and incubated at 37 °C for 8 h. Viable colony units of *E. coli* and *S. aureus* were photographed and counted.

In vitro antibacterial rate assay

The antibacterial activity of the gels was further studied using the optical density (OD_{600}) method. The 200 µL of the bacterial suspension was added to each well, and the samples were incubated at 37 °C in the dark for 12 h for *E. coli* and 24 h for *S. aureus*, respectively. The OD value of the bacterial solution after dark incubation for 12 h at 37 °C was the control. The bactericidal ratio was determined using the following equation:

Antibacterial rate (%)

$$= \frac{(\text{Control group OD} - \text{Experimental group OD})}{\text{Control group OD}} * 100\%$$

In vivo implantation of hydrogel

Medical Sodium Hyaluronate Gels (HA gels) were purchased from a local hospital as control group to evaluate the in vivo toxicity of COB hydrogels. Male ICR mice (8–9 weeks) were obtained from Laboratory Animals Center of Zhejiang Chinese Medicine University. All the animals were anaesthetized by an intraperitoneal injection of 0.3% sodium pentobarbital (0.1 ml/10 g) and their dorsal regions were shaved and sterilized. The mice were injected subcutaneously with 200 µL hydrogels (HA gels, COB_0 gels, and $COB_{1.5}$ gels) by a dual-barrel syringe. The tissue around the hydrogel was removed 3 and 7 days later.

Histological analysis

On the 3th and 7th day after initial treatment, tissue around hydrogels was excised, maintained in cold 4% paraformaldehyde overnight. Skin tissue was sectioned into 5-µm thickness slices for Hematoxylin and Eosin (H&E) (Wuhan Servicebio Technology Co., Ltd. Wuhan, China) staining. All procedures for the stains were followed the protocols described in our previous studies. The tissue slices for H&E and Masson's trichrome were observed by a digital pathology slide scanning system (C13210-01, Hamamatsu, Japan).

In vivo biosafety study

H&E staining was used to evaluate the biocompatibility of hydrogels. After 7 days, all mice were sacrificed and the major organs (heart, liver, spleen, lung and kidney) from each group were harvested for histological staining. All sections were observed by a digital pathology slide scanning system. The Animal experiment protocol listed above had been reviewed and approved by Laboratory animal management and ethics committee of Zhejiang Chinese Medicine University (approval no. IACUC202104-0138).

All data were analyzed and visualized by GraphPad Prism 8.0.1 (LLC, USA). All values are shown as the mean±SD and every experiment was repeated at least three times. One-way ANOVA was performed to compare the data with paired samples, and two-way ANOVA was applied for multiple group comparisons. *p value<0.05 was considered statistically significant.

Result and discussion

The synthesis and characterization of COB hydrogels

As shown in Fig. S1a, the BGNs were uniformly spherical and exhibited favorable monodispersibility. The average particle diameter of the BGNs was approximately 91.95±12.83 nm and exhibited small amounts of aggregation (Fig. S1b, supporting information). The result was consistent with those of Dynamic light scattering (DLS, S1e), which showed 589 nm. As shown in Fig. S1c, the BGNs developed in this study exhibited amorphous structures with a broad peak at $2\theta=23°$. Fig. S1d showed the N_2 absorption–desorption isotherm plots and pore-size distributions of the BGN. The BGNs showed a Brunauer–Emmett–Teller (BET) surface area of 221.35 m^2/g and a total pore volume of 0.149 cm^3/g, contributed by a remarkable number of micropores centered at 4 nm (illustration), which is also in good agreement with the N_2 sorption results (Table S1, supporting information). In addition, the zeta potential of BGN was approximately -20 mV (Fig. S1f). These results indicated that homogeneous monodisperse BGNs were successfully synthesized and that BGNs have similar properties to mesoporous materials.

The COB hydrogel sample was extruded into the bottle, changed from flowing to hydrogel state, and inverted for 5 s without falling, which was defined as gelation time. The gelation time of $COB_{1.5}$ was faster than that of COB_0 (18 s) and COB_1 (9 s), at 7 s. SEM was performed to analyze the micro structure of COB_0, $COB_{0.5}$, COB_1 and $COB_{1.5}$ hydrogels. All these hydrogels exhibited porous structure, but $COB_{0.5}$, COB_1 and $COB_{1.5}$ hydrogels showed particle attachment, which may be due to the function of BGN

particles. The red arrows indicated BGN, and they were distributed in the hydrogel skeleton. Compared with COB_0 (inset in Fig. 1d), the X-ray energy spectrum analysis (EDS) of $COB_{1.5}$ demonstrated the composition and verified the presence of BGNs (Fig. 1d and Fig. S3, supporting information). In addition, all hydrogels demonstrated typical amorphous structures, although a broad peak was observed at 23° (Fig. 1e). As shown in Fig. 1f, FTIR spectra of COB hydrogels in the Amide I region (1617 cm^{-1}), which ranged from 1580 to 1720 cm^{-1}, indicating the COB gels was confirmed by Schiff base reaction. The broad bands at approximately 820 cm^{-1} and 480 cm^{-1} were associated with the stretching vibration of Si–O [29] (Fig. 1g). The band at 3300–3600 cm^{-1} was attributed to the vibration of hydroxyl groups (–OH). The characteristic bands of Si–O and –OH were significantly enhanced as the increase of BGN content, indicating that the introduction of BGN might enhance the intermolecular hydrogen bonding.

In vitro biomineralization bioactivity

It has been reported that BGN-based biomaterials have high biomineralization activity [26]. Fig. S4a showed the biominerialization activity of BGN nanocomposites by analyzing the apatite forming in SBF. Obvious biommineralized layer structure was observed on the surface, during the soaking time of 1 and 3 days. The P and Ca peak (EDS) was increased gradually as the immersing time in SBF (Fig. S4c and 4d, supporting information) [33]. Compared with COB_0, an obvious biommineralized layers were observed on the surface of BGNs in the $COB_{1.5}$ hydrogels (Fig. S4e and S4f). The FTIR spectra further confirmed that the formation of biological apatite nanocrystals which had the characteristic bands of at 1040 cm^{-1}, 1424 cm^{-1} (Fig. S4g and Fig.S4h, supporting information) [26].

X-ray photoelectron spectroscopy

X-ray photoelectron spectroscopy (XPS) analysis provided relevant information about the type of functional groups on the hydrogels' surface. Obviously, it could be observed that O1s, N1s, C1s, Si2p and Ca2p exist in $COB_{1.5}$ hydrogels from Fig. 2a, while three characteristic peaks of C1s, O1s, and N1s were present in COB_0 gels. The existence of Ca and Si elements in $COB_{1.5}$ hydrogels were ascribed to BGN.
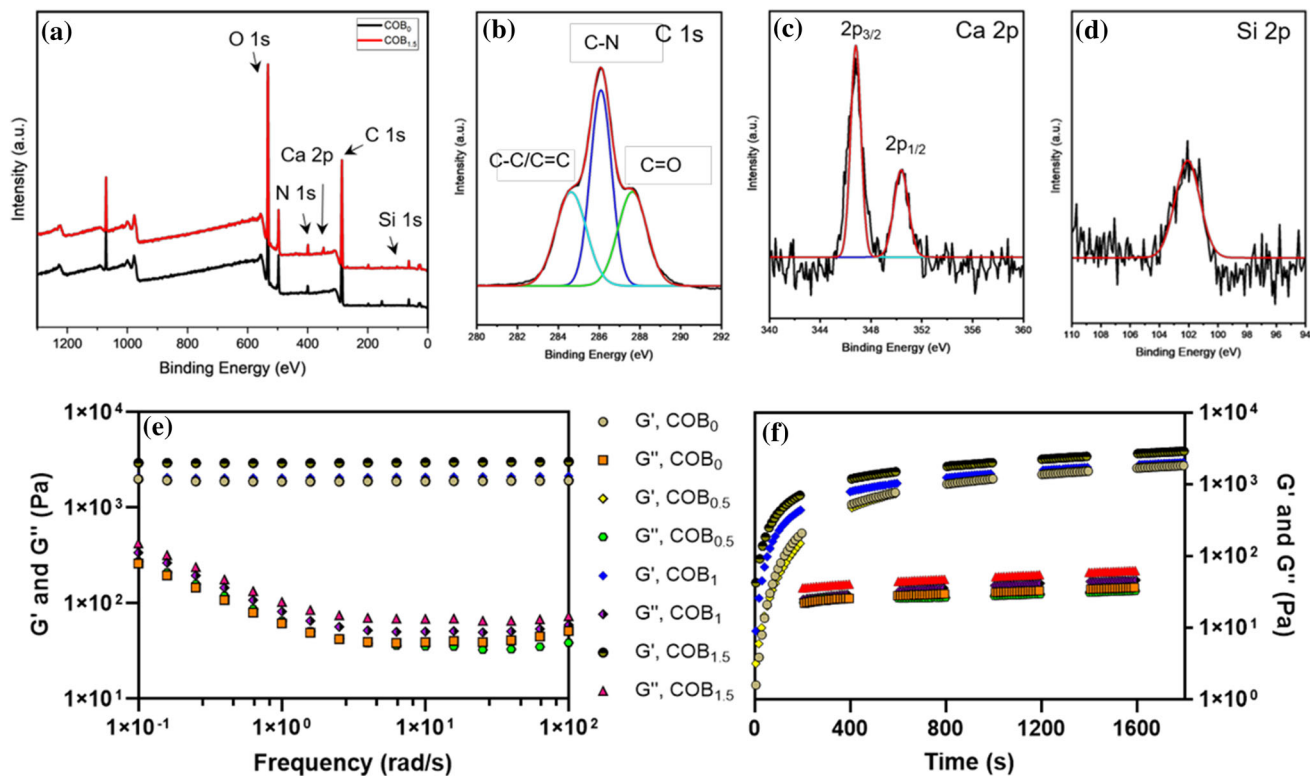
Figure 2 XPS spectra images of hydrogels. **a** XPS wide scan of COB_0 and $COB_{1.5}$ hydrogels. **b** C 1 s spectra **c** Ca 2p and **d** Si 2p of $COB_{1.5}$ hydrogels. **e** Rheological properties of COB hydrogels. **f** Cyclic G′ and G″ values of the hydrogel for a fixed angular frequency (10 rad/s) and different time sweeping.

Furthermore, the C1s peak of $COB_{1.5}$ hydrogels could be divided into three peaks at 284.6 eV, 285.8 eV and 287.6 eV, corresponding to C–C/C=C, C–N and C=O respectively (Fig. 2b) [34]. Figure 2c showed the high-resolution Ca2p spectra of $COB_{1.5}$ gels, and the peaks at 350.4 eV and 346.8 eV confirmed the hydroxylation of the CaO surface. The peak at 102.2 eV suggesting the successful deposition of the Si–O (Fig. 2d) [33, 35].

Mechanical property and Rheological analysis

As shown in Fig. S5, the compressive fracture stress of $COB_{1.5}$ hydrogels was 174.27 ± 36.92 kPa which was significantly superior to COB_0, $COB_{0.5}$ and COB_1 groups, respectively (58.72 ± 16.90 kPa, 94.15 ± 22.22 kPa, 134.51 ± 26.06 kPa). Investigation of the stress of the gels with BGN showed a substantial increase in stress in comparison to COB_0 hydrogels, which demonstrates that the BGN-containing hydrogel was able to withstand higher stress. This can be attributed to the stronger interaction of BGN

with hydrogel network, so the more BGN added to the gel, the higher the compressive stress.

Further, we carried out rheological studies to determine COB hydrogels' viscoelastic behavior to testify the effects of the incorporating BGN. The results showed that the storage modulus (G′) were higher than the loss modulus (G″) in all the cases studied, which confirming the formation of highly stable and elastic hydrogels (Fig. 2e). With that, the storage modulus (G′) of the $COB_{1.5}$ hydrogels was 3046.28 Pa which was significantly superior to COB_0, $COB_{0.5}$ and COB_1 groups, respectively (1920.18 Pa, 1968.99 Pa and 2138.66 Pa). The results of oscillatory rheology show that the G′ of BGN-added hydrogels is larger than that of the hydrogels without nanoparticles, and the strength increases with the increase of BGN content. This is not surprising, as BGN is expected to interact with the gel network due to the certain surface area each particle has (221.352 m^2/g) [36]. Moreover, we fixed angular frequency to 10 rad/s and temper temperature (25 °C) to investigate the influence of time on sol–gel transition kinetics of the hydrogel. When hydrogels with BGN
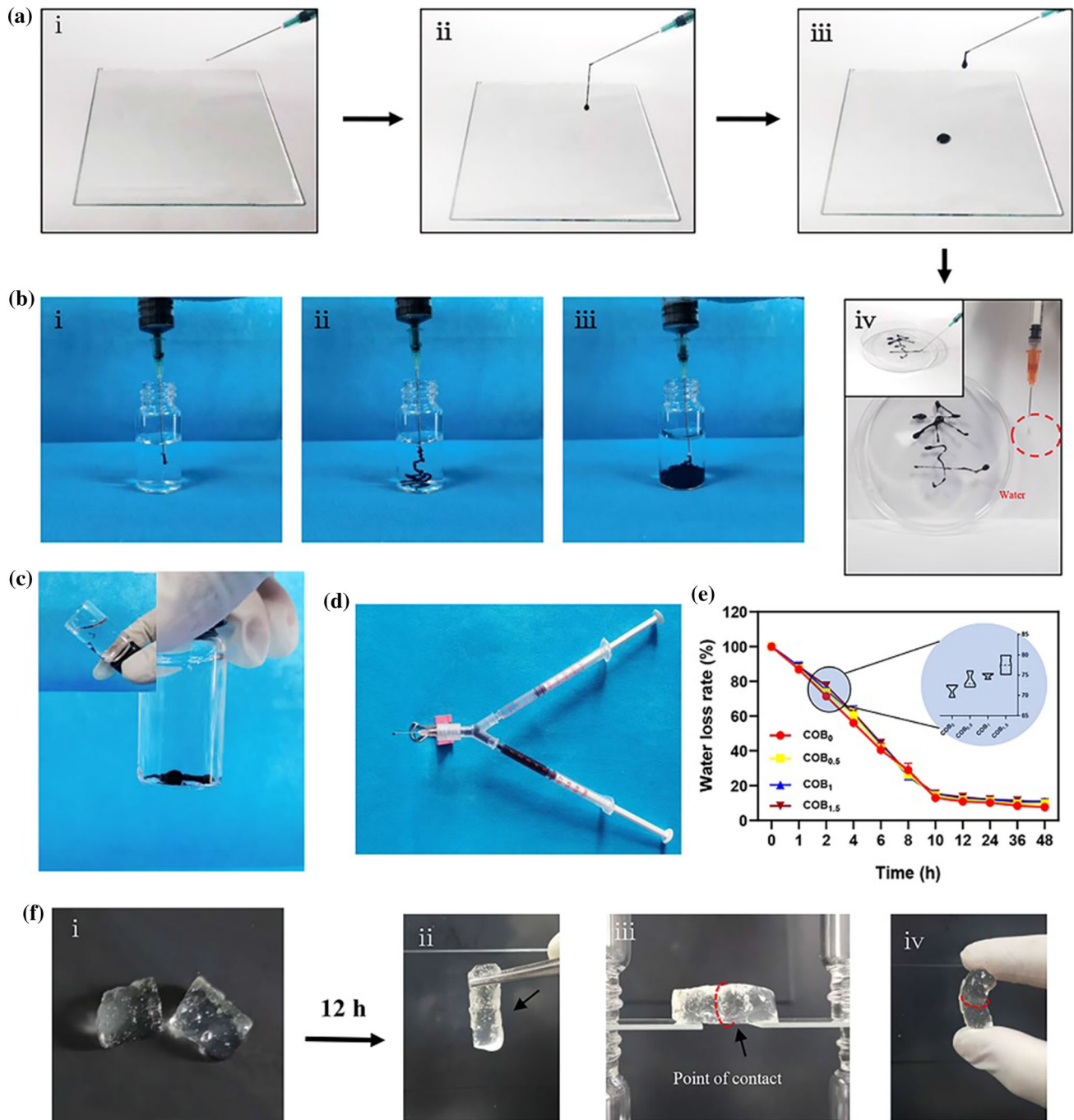
Figure 3 Injectability and self-healing performance of COB hydrogels. **a** Photographs of black ink stained COB_0 at different stages in air (**i**–**iv**) of injectability. Inset in **iv** shows the image of "李" not falling from the dish, freely dripping water as a control. **b** the $COB_{1.5}$ hydrogels were extruded into PBS at different stages. **c** Hydrogels showed great stability, and even before and after (illustration) the shock, the gels did not dissolve. **d** Neutralized OCM/black ink suspension and 15% CMCs/1.5% BGN were loaded in separate syringes respectively and mixed rigorously with a joint connector. **e** The water loss rate of COB hydrogels. The illustration showed the water loss rate after 2 h. **f** Visual evidence of self-healing COB_0 hydrogel: **i** the cut sample of hydrogel, **ii** self-healed could withstand its own weight without falling, **iii** two parts of the healed hydrogel on a bridge support and **iv** self-healed sample bent in "U" shape by fingers. The point of contacts was encircled in (**iii**) and (**iv**).

($COB_{0.5}$, COB_1 and $COB_{1.5}$) were subjected to a small amplitude oscillatory shear (strain=2.5%), G′ was greater than G″ in a very short time (5 s), while COB_0 was within 20 s. These results proved the shorten of gelation time by the inclusion of BGN.

The injectable and self-healing of the hydrogels

To demonstrate the injectability of the COB hydrogels, COB_0 was stained with black ink to observe the process. The COB_0 gel in the syringe could easily pass through the needle. The gel retained its behavior even after passing through the needle; Fig. 3a shows the different stages. To meet the requirements of the internal gel, the hydrogels also need to retain their shape after being extruded into a water environment. As shown in Fig. 3d, the $COB_{1.5}$ hydrogels were extruded into 37 °C PBS using a syringe, and Fig. 3b: i–iii showed the different stages. The gel retained its gelatinous behavior, even in PBS (Fig. 3c). Hydrogels need to possess self-healing properties to maintain their integrity and functionality. Two pieces of the fractured COB_0 hydrogel (Fig. 3f: i) were placed in close proximity in a closed environment to minimize water evaporation from the gel. These pieces rejoined within 12 h to form a single hydrogel. The self-healing point can be observed in the left scar (Fig. 3f, ii). Furthermore, the self-healing gel could withstand its own weight without falling. The hydrogel was placed on the bridge and bent into a "U" shape (Fig. 3f: iv).

Furthermore, the compressive stress–strain curves showed that the self-healed hydrogel share similar profiles with the original samples (Fig. S6, supporting information). Fracture pressure of self-healed hydrogel was 53.33 ± 14.72 kPa, while the original samples was 64.53 ± 15.20 kPa (illustration). And the self-healing efficiency of COB_0 hydrogels was $82.74 \pm 10.36\%$. The self-healing ability of hydrogels was attributed to weak noncovalent hydrogen bonds and dynamic covalent Schiff base networks in hydrogels [9]. In addition, Water loss rate experiments showed that the hydrogels lost their water more than 75% in 24 h (Fig. 3e). The illustration showed the water loss rate after 2 h, which resulted in $71.49 \pm 1.7\%$, $73.67 \pm 2.1\%$, $74.88 \pm 0.7\%$ and $77.50 \pm 2.3\%$ corresponding to COB_0, $COB_{0.5}$, COB_1 and $COB_{1.5}$ respectively (inset). The rate of water loss of hydrogels was proportional to the content of BGN in a short space of time. We speculated that this is due to the presence of

Figure 4 Schematic (**a**) and representative image (**b**) of the ▶ bonding strength measurements. **c** The bonding strength and **d** stress–strain curves of COB hydrogels and CMCs. (*, $p<0.05$, **, $p<0.01$, n=4). **e** UV spectrum of Dox as control, supernatant of COB_0, $COB_{0.5}$, COB_1 and $COB_{1.5}$ after 48 h. **f** Histogram showing the percent of Dox loaded on different gels. **g** Histogram showing the Dox release from COB_0, $COB_{0.5}$, COB_1 and $COB_{1.5}$ as a function of time in PBS at pH 7.4. **h** Percent of degradation of COB hydrogel in PBS at pH 7.4 as a function of time. (Error bars indicated means $\pm$ SD. Data analyzed by one-way ANOVA. *, $p< 0.05$, **, $p<0.01$ and ***, $p<0.001$).

unacceptable BGNs. In addition, the equilibrium water content (EWC) of COB hydrogels was $83.10 \pm 4.5\%$, $81.67 \pm 2.9\%$, $82.60 \pm 2.37\%$, $84.45 \pm 2.36\%$, respectively. And no obvious EWC difference was discovered among those COB hydrogels, indicating that BGN did not influence the water content of COB hydrogels (Fig. S7, supporting information).

Adhesion of hydrogels

One of the main concerns for the practical application of hydrogels is the strength of its binding to the tissue around the wound. In this study, pig skin was used as a representative tissue because it is biologically similar to human dermis. The adhesion test method is shown in Fig. 4a and b. The bonding strength of CMCs was only approximately 46.2 kPa, and stress at fracture was 16.86%, which was substantially lower than that of COB hydrogels. As shown in Fig. 4c and d, the bonding strength for the $COB_{1.5}$ hydrogels was 96.5 kPa and the stress at fracture was 96.5%, which was significantly superior to COB_0 and $COB_{0.5}$ hydrogels (74.75 and 73.05 kPa, respectively). We speculated about the reasons for this adhesive behavior is a consequence of the increased ability of the small nanoparticles to both lie on the contours of the gel surface and not interact with each other [36].

Drug release from the hydrogel

In this work, Dox was chosen as model drug to evaluate the capacity of COB hydrogels in drug loading. The results showed that $COB_{1.5}$ hydrogel had good drug encapsulation rate and sustained release ability. The drug loading efficiency and release rates of COB_0, $COB_{0.5}$, COB_1 and $COB_{1.5}$ were $25.05 \pm 8.0\%$ and $21.30 \pm 1.44\%$, $23.31 \pm 13.79\%$ and $24.37 \pm 3.0\%$; $47.50 \pm 4.79\%$ and $37.83 \pm 2.77\%$; $64.10 \pm$
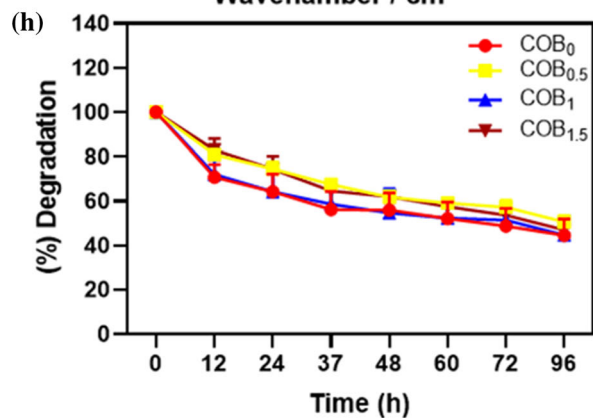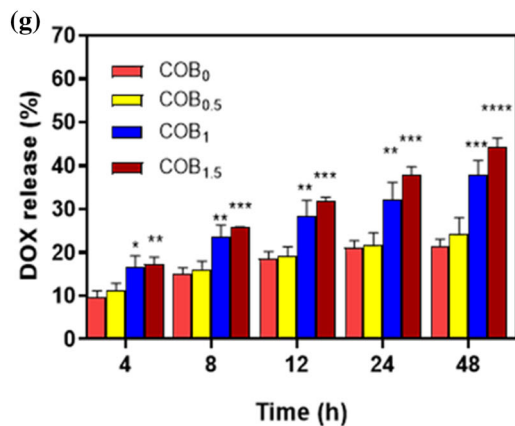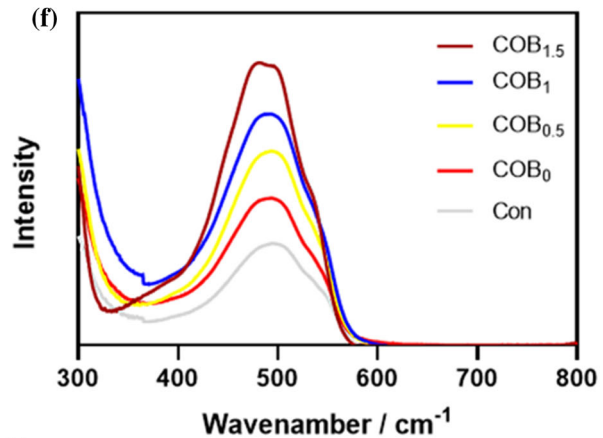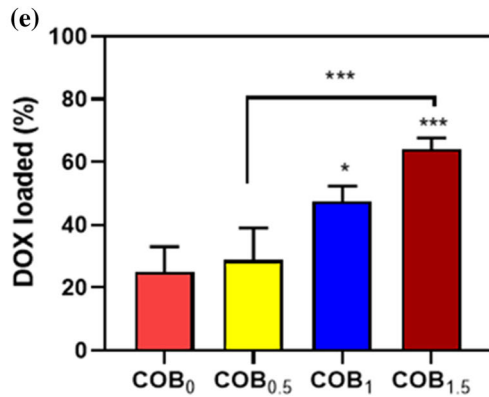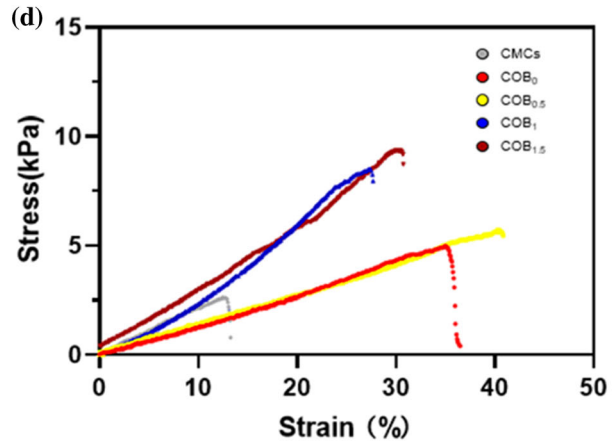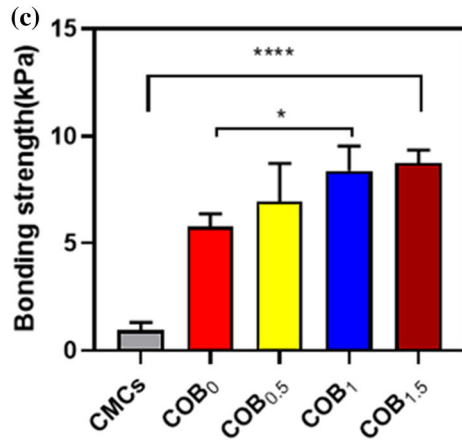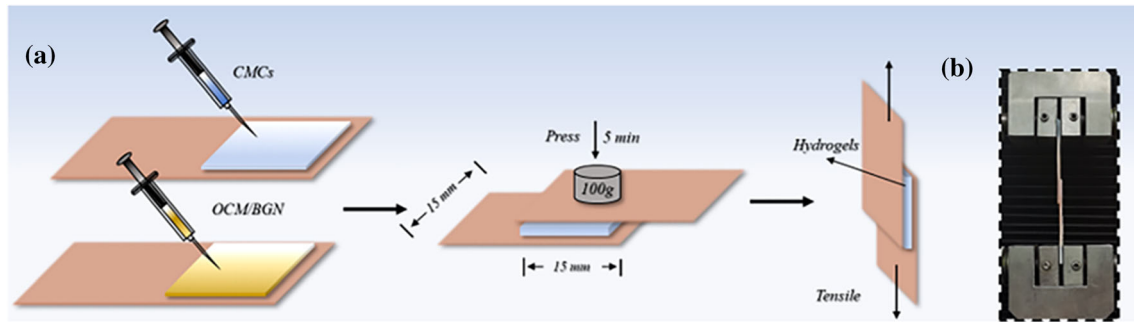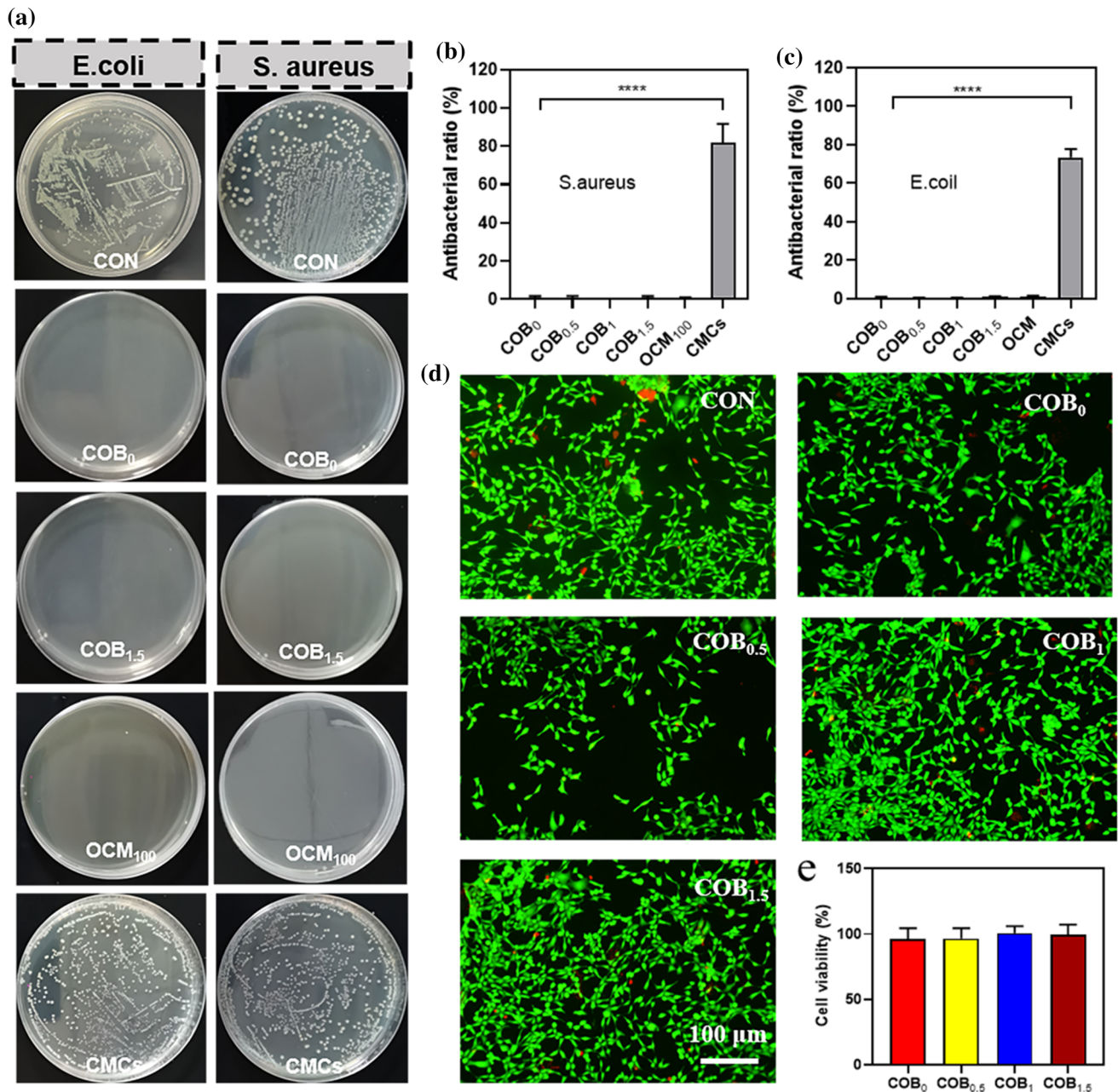
Figure 5 **a** Antibacterial properties of hydrogels against various microbes. Qualitative test of the antibacterial ability of hydrogels to the **b** *S. aureus* (Gram-positive) and **c** *E. coli* (Gram-negative). ****$p<0.0001$, n=3. **d** Live/dead cell viability assay. NIH 3T3 cells were treated with different COB hydrogels. The live (green) and dead (red) cells were stained with fluorescent dyes and observed under a fluorescent microscope. Scale bar=100 μm. **e** In vitro evaluation of the cytocompatibility of the prepolymer solution in certain concentrations. Cells cultured with DMEM were used as control. CCK-8 assay for evaluation of cytotoxicity of different sample. (*, $p<0.05$, **, $p<0.01$ and ***, $p<0.001$).

3.35% and 44.28±1.62%, respectively. Such results are attributed to the charge interaction between the negatively charged BGN (Fig. S1f) and the positively charged DOX [37]. Therefore, it is a suitable candidate material for cancer drug delivery.

In vitro degradation of the hydrogels

Degradation ability is an important characteristic of hydrogels. Investigation on the hydrogel degradation was completed by checking the weight loss percent of
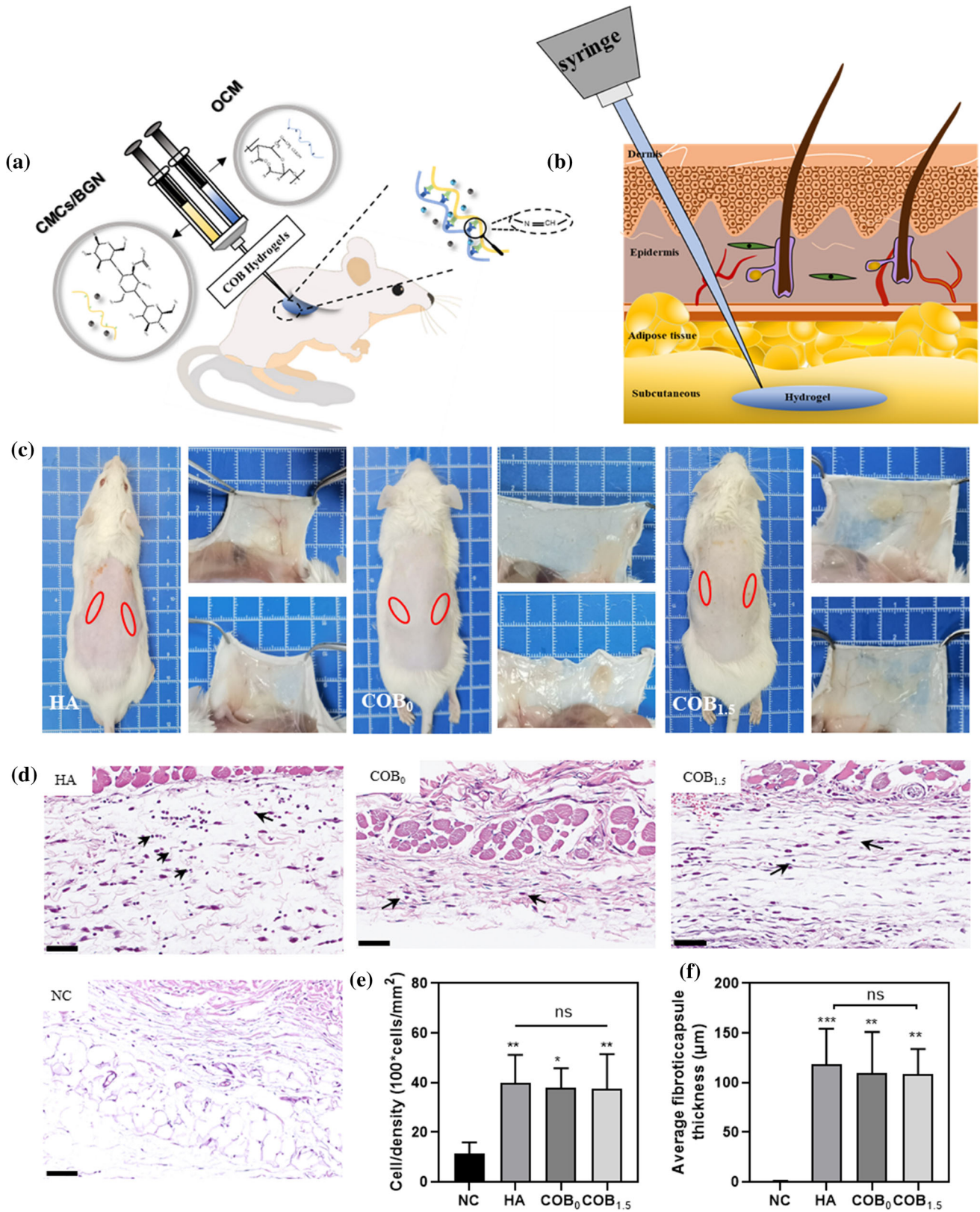
◄ **Figure 6 a** Schematic illustration of COB hydrogel injection in vivo. **b** The biosafety of hydrogels was evaluated by subcutaneous injection. **c** Representative images of ICR mice after injection of different hydrogels (day 7). The inset showed the typical gross morphologies of hydrogel blocks before sample collection. **d** Representative image of H&E staining of tissue sections of hydrogels injected subcutaneously in mice for one week. The arrows pointed to the inflammatory cells. Scale bars= 50 μm. **e** Infiltrated cells and average fibrous capsule thickness **f** statistics of the surrounding subcutaneous tissues. The number of inflammatory cells was calculated according the following equation: relative cell number=(100*cell number)/relative area. n>3. *$p<0.05$ and **$p<0.01$.

hydrogels soaking in PBS at pH 7.4. We attributed the degradability of COB hydrogels to dynamic cross-linking induced by Schiff base. In vitro degradation testing showed that COB_0 hydrogels has faster degradation rate in PBS as compared to other hydrogels with BGN at the same OCM concentration. After hydrogels were immersed in PBS for 96 h, the degradation rate of COB_0 was $44.45\pm7.56\%$, while that of other hydrogels was 53.02 ± 2.4, $53.56\pm2.32\%$ and $56.36\pm1.31\%$, respectively (Fig. 4g). Data analyzed by one-way ANOVA for each time period. There were significant differences among COB_0, COB_1 and $COB_{1.5}$ hydrogels within 48 h. That's because the existence of no incompatible BGN. We attributed the degradability of cellulose derivatives-based hydrogels to dynamic cross-linking induced by Schiff base.

Antibacterial properties and Cytotoxicity

The antibacterial ability of COB hydrogels to *Escherichia coli* and *Staphylococcus aureus* was also investigated. As shown in Fig. 5a, COB_0, $COB_{1.5}$ and OCM_{100} completely inhibited the growth of bacterial colonies in culture medium including gram-positive and gram-negative bacteria, indicating the excellent antibacterial property of COB gels was attributed to aldehyde groups form OCM_{100}. In addition, the results of antibacterial rate experiment also proved that COB hydrogel had good antibacterial properties (Fig. 5b and c). The results showed that the antibacterial activity of the COB hydrogel was mainly derived from OCM, which might be caused by the reaction between the aldehyde and amino groups in the bacterial cell wall protein, resulting in cell wall destruction and content leakage [13].

To further evaluate the cytotoxicity of COB hydrogels, cell proliferation and live-death staining studies were performed on NIH/3T3 cells. As shown in Fig. 5d, the results of cell viability staining showed that the hydrogel was non-toxic, whose result was consistent with CCK-8 cell proliferation (Fig. 5e). The above results of cytocompatibility experiments showed that COB hydrogel had good biocompatibility and met the safety requirements of drug administration in vivo.

In vivo biocompatibility

To test the biocompatibility of COB hydrogels, the rejection in vivo and early infection by subcutaneously injecting (Fig. 6b) both COB_0, $COB_{1.5}$ and Hyaluronic acid (HA) hydrogels into mace for one week. The mice without any implants were used as normal controls (NC). As shown in Fig. 6c, all hydrogels including COB_0, $COB_{1.5}$ and HA were successfully injected through syringe without clogging. Figure 6d showed a representative image of H&E staining of the tissue sections of the hydrogels. Compared with the NC and HA groups, $COB_{1.5}$ group showed significantly low numerous inflammatory cells and fibrous capsule thickness (Fig. 6e and f), indicating that COB hydrogels have good biocompatibility. We further studied collagen deposition using Masson's trichrome staining. As shown in Fig. S8, the HA hydrogel was encapsulated by a much denser collagen capsule, whereas the COB_0 and $COB_{1.5}$ hydrogels showed fewer sacs with loosely distributed collagen. In addition, collagen sacs gradually formed around the tissue and around the hydrogel due to inflammatory stimulation. This result further demonstrated that COB hydrogel scaffolds exhibit more effective safety than conventional hydrogels and can be applied to in vivo tissue engineering.

H&E staining of major organs (heart, liver, spleen, lung, and kidney) of the corresponding mice was also investigated for an in-depth evaluation. Notably, no detectable damage was found in the H&E staining results in the COB groups compared with that in the HA group (Fig. S9, supporting information), confirming the biocompatibility of COB hydrogels in vivo. The results suggested that the COB hydrogel scaffold exerted desirable biocompatibility in vivo and showed great potential for replacing commercial hydrogels such as HA.

Conclusions

In summary, we have prepared an injectable multifunctional hydrogel scaffold with self-healing, drug-loading, and degradation capabilities, which is important for tissue engineering and drug delivery applications. The hydrogels are prepared by mixing carboxymethyl chitosan and cellulose derivatives, in the presence of a small amount of BGN. The differential drug release of COB hydrogels showed interesting drug loading characteristics owing to the porous nature of the gels and the charge attraction of BGN and DOX, which indicating their advantages in the field of drug delivery. Hydrogels also exhibited excellent injectability and plasticity, because of the reversibility of dynamic Schiff base interaction. These suggested that they can be easily operated with syringes or other delivery systems during interventional surgery. In vitro experiments proved that the hydrogel had excellent biocompatibility, antibacterial property and degradability. Moreover, the hydrogel scaffold had no cytotoxicity and mild inflammatory reaction in vivo, which could find potential advantages in the field of minimally invasive surgery. Combining these features with low cost and ease of synthesis, this injectable self-healing hydrogel is a promising candidate for tissue engineering and drug delivery applications.

Acknowledgements

Author contributions

SL contributed to conceptualization, formal analysis, investigation, writing—original draft, funding acquisition. LX contributed to formal analysis, supervision. XW and WM contributed to data curation, formal analysis, investigation. YG contributed to supervision, validation. JW and HX contributed to writing—review and editing, supervision. JH, and HF contributed to formal analysis. LJ and QS contributed to formal analysis, funding acquisition, supervision.

Declarations

Supplementary Information: The online version contains supplementary material available at https://doi.org/10.1007/s10853-023-08393-8.

References

[1] Guo Y, Bae J, Fang Z, Li P, Zhao F, Yu G (2020) Hydrogels and hydrogel-derived materials for energy and water sustainability. Chem Rev 120:7642–7707. https://doi.org/10.1021/acs.chemrev.0c00345

[2] Huang Q, Zou Y, Arno MC et al (2017) Hydrogel scaffolds for differentiation of adipose-derived stem cells. Chem Soc Rev 46:6255–6275. https://doi.org/10.1039/c6cs00052e

[3] Nezhad-Mokhtari P, Akrami-Hasan-Kohal M, Ghorbani M (2020) An injectable chitosan-based hydrogel scaffold containing gold nanoparticles for tissue engineering applications. Int J Biol Macromol 154:198–205. https://doi.org/10.1016/j.ijbiomac.2020.03.112

[4] Rizzo F, Kehr NS (2021) Recent advances in injectable hydrogels for controlled and local drug delivery. Adv Healthc Mater 10:e2001341. https://doi.org/10.1002/adhm.202001341

[5] Gao F, Jiao C, Yu B, Cong H, Shen Y (2021) Preparation and biomedical application of injectable hydrogels. Mater Chem Front 5:4912–4936. https://doi.org/10.1039/d1qm00489a

[6] Vashahi F, Martinez MR, Dashtimoghadam E et al (2022) Injectable bottlebrush hydrogels with tissue-mimetic mechanical properties. Sci Adv 8:eabm2469. https://doi.org/10.1126/sciadv.abm2469

[7] Colucci F, Mancini V, Mattu C, Boffito M (2021) Designing multifunctional devices for regenerative pharmacology based on 3D scaffolds, drug-loaded nanoparticles, and thermosensitive hydrogels: a proof-of-concept study. Pharmaceutics. https://doi.org/10.3390/pharmaceutics13040464

[8] Kai Chen ZW, Liu Y, Yuan Y, Liu C (2021) Injectable double-crosslinked adhesive hydrogels with high mechanical resilience and effective energy dissipation for joint woun. Adv Funct Mater. https://doi.org/10.1002/adfm.202109687

[9] Lei Zhou CD, Fan L, Jiang Y, Liu C, Zhou Z, Pengfei Guan Yu, Tian JX, Li X, Luo Y, Peng Yu, Ning C, Tan G (2021) Injectable self-healing natural biopolymer-based hydrogel adhesive with thermoresponsive reversible adhesion for minimally invas. Adv Funct Mater 31:2007457. https://doi.org/10.1002/adfm.202007457

[10] Su H, Zheng R, Jiang L, Zeng N, Yu K, Zhi Y, Shan S (2021) Dextran hydrogels via disulfide-containing Schiff base formation: synthesis, stimuli-sensitive degradation and release behaviors. Carbohydr Polym 265:118085–118096. https://doi.org/10.1016/j.carbpol.2021.118085

[11] Li S, Pei M, Wan T et al (2020) Self-healing hyaluronic acid hydrogels based on dynamic Schiff base linkages as biomaterials. Carbohydr Polym 250:116922–16950. https://doi.org/10.1016/j.carbpol.2020.116922

[12] Chen Y, Ye M, Song L et al (2020) Piezoelectric and photothermal dual functional film for enhanced dermal wound regeneration via upregulation of Hsp90 and HIF-1α. Appl Mater Today 20: 100756–100772. https://doi.org/10.1016/j.apmt.2020.100756

[13] Pang J, Bi S, Kong T et al (2020) Mechanically and functionally strengthened tissue adhesive of chitin whisker complexed chitosan/dextran derivatives based hydrogel. Carbohydr Polym 237:116138–116163. https://doi.org/10.1016/j.carbpol.2020.116138

[14] Salleh KM, Zakaria S, Sajab MS, Gan S, Kaco H (2019) Superabsorbent hydrogel from oil palm empty fruit bunch cellulose and sodium carboxymethylcellulose. Int J Biol Macromol 131:50–59. https://doi.org/10.1016/j.ijbiomac.2019.03.028

[15] Pagano C, Calarco P, Di Michele A et al (2021) Development of sodium carboxymethyl cellulose based polymeric microparticles for in situ hydrogel wound dressing formation. Int J Pharm 602:120606. https://doi.org/10.1016/j.ijpharm.2021.120606

[16] Sheng Y, Gao J, Yin ZZ, Kang J, Kong Y (2021) Dual-drug delivery system based on the hydrogels of alginate and sodium carboxymethyl cellulose for colorectal cancer treatment. Carbohydr Polym 269:118325–118333. https://doi.org/10.1016/j.carbpol.2021.118325

[17] Li H, Wu B, Mu C, Lin W (2011) Concomitant degradation in periodate oxidation of carboxymethyl cellulose. Carbohyd Polym 84:881–886. https://doi.org/10.1016/j.carbpol.2010.12.026

[18] Lee JH (2018) Injectable hydrogels delivering therapeutic agents for disease treatment and tissue engineering. Biomater Res 22:27–1. https://doi.org/10.1186/s40824-018-0138-6

[19] Kumar R, Kehr NS (2022) 3D-printable oxygen- and drug-carrying nanocomposite hydrogels for enhanced cell viability. Nanomaterials (Basel). https://doi.org/10.3390/nano12081304

[20] Reker D, Rybakova Y, Kirtane AR et al (2021) Computationally guided high-throughput design of self-assembling drug nanoparticles. Nat Nanotechnol 16:725–733. https://doi.org/10.1038/s41565-021-00870-y

[21] Motealleh A, Kart D, Czieborowski M, Kehr NS (2021) Functional nanomaterials and 3D-printable nanocomposite hydrogels for enhanced cell proliferation and for the reduction of bacterial biofilm formation. ACS Appl Mater Interfaces 13:43755–43768. https://doi.org/10.1021/acsami.1c13392

[22] Li S, Chen A, Chen Y et al (2020) Lotus leaf inspired antiadhesive and antibacterial gauze for enhanced infected dermal wound regeneration. Chem Eng J. https://doi.org/10.1016/j.cej.2020.126202

[23] Ben Haddada M, Gerometta E, Chawech R et al (2020) Assessment of antioxidant and dermoprotective activities of gold nanoparticles as safe cosmetic ingredient. Colloids Surf B Biointerfaces 189:110855–110879. https://doi.org/10.1016/j.colsurfb.2020.110855

[24] Viswanathan K, Monisha P, Srinivasan M, Swathi D, Raman M, Dhinakar Raj G (2016) Chlorhexidine-calcium phosphate

nanoparticles—polymer mixer based wound healing cream and their applications. Mater Sci Eng C Mater Biol Appl 67:516–521. https://doi.org/10.1016/j.msec.2016.05.075

[25] Schumacher M, Habibovic P, van Rijt S (2021) Mesoporous bioactive glass composition effects on degradation and bioactivity. Bioact Mater 6:1921–1931. https://doi.org/10.1016/j.bioactmat.2020.12.007

[26] Li Y, Guo Y, Niu W et al (2018) Biodegradable multifunctional bioactive glass-based nanocomposite elastomers with controlled biomineralization activity, real-time bioimaging tracking, and decreased inflammatory response. ACS Appl Mater Interfaces 10:17722–17731. https://doi.org/10.1021/acsami.8b04856

[27] Kim TH, Kang MS, Mandakhbayar N, El-Fiqi A, Kim HW (2019) Anti-inflammatory actions of folate-functionalized bioactive ion-releasing nanoparticles imply drug-free nanotherapy of inflamed tissues. Biomaterials 207:23–38. https://doi.org/10.1016/j.biomaterials.2019.03.034

[28] Granel H, Bossard C, Nucke L et al (2019) Optimized bioactive glass: the quest for the bony graft. Adv Healthc Mater 8:e1801542. https://doi.org/10.1002/adhm.201801542

[29] Hu Q, Li Y, Miao G, Zhao N, Chen X (2014) Size control and biological properties of monodispersed mesoporous bioactive glass sub-micron spheres. RSC Adv 4:22678–22687. https://doi.org/10.1039/c4ra01276c

[30] Zhu H, Mei X, He Y et al (2020) Fast and high strength soft tissue bioadhesives based on a peptide dendrimer with antimicrobial properties and hemostatic ability. ACS Appl Mater Interfaces 12:4241–4253. https://doi.org/10.1021/acsami.9b18720

[31] Wei Y, Wang H, Zhang X, Liu C (2021) Ammonia-assisted hydrothermal carbon material with schiff base structures synthesized from factory waste hemicelluloses for Cr(VI) adsorption. J Environ Chem Eng 9:106187–06196. https://doi.org/10.1016/j.jece.2021.106187

[32] Tong X, Tian Z, Sun J, Tung V, Kaner RB, Shao Y (2021) Self-healing flexible/stretchable energy storage devices. Mater Today 44:78–104. https://doi.org/10.1016/j.mattod.2020.10.026

[33] Fujimori Y, Zhao X, Shao X, Levchenko SV, Nilius N, Sterrer M, Freund H-J (2016) Interaction of water with the CaO(001) surface. J Phys Chem C 120:5565–5576. https://doi.org/10.1021/acs.jpcc.6b00433

[34] Zhang Y, Zhang Z, Li J, Sui G (2019) (3-aminopropyl) triethoxysilane grafted poly(dopamine)@Fe_3O_4 nanoparticles and their epoxy composites for functional application. Compos B Eng 169:148–156. https://doi.org/10.1016/j.compositesb.2019.04.012

[35] Bozorgi B, Karimi-Sabet J, Khadiv-Parsi P (2022) The removal of N_2O from gas stream by catalytic decomposition over Pt-alkali metal/SiO_2. Environ Technol Innov. https://doi.org/10.1016/j.eti.2022.102344

[36] Arno MC, Inam M, Weems AC et al (2020) Exploiting the role of nanoparticle shape in enhancing hydrogel adhesive and mechanical properties. Nat Commun 11:1420–1429. https://doi.org/10.1038/s41467-020-15206-y

[37] Pereira TA, Ramos DN, Lopez RF (2017) Hydrogel increases localized transport regions and skin permeability during low frequency ultrasound treatment. Sci Rep 7:44236–44246. https://doi.org/10.1038/srep44236

Publisher's Note Springer Nature remains neutral with regard to jurisdictional claims in published maps and institutional affiliations.